ADVANCED FUNCTIONAL MATERIALS
www.afm-journal.de

www.MaterialsViews.com

Electrostatic Self-Assembly of Nanosized Carbon Nitride Nanosheet onto a Zirconium Metal–Organic Framework for Enhanced Photocatalytic CO_2 Reduction

*Li Shi, Tao Wang, Huabin Zhang, Kun Chang, and Jinhua Ye**

UiO-66, a zirconium based metal–organic framework, is incorporated with nanosized carbon nitride nanosheets via a facile electrostatic self-assembly method. This hybrid structure exhibits a large surface area and strong CO_2 capture ability due to the introduction of UiO-66. We demonstrate that electrons from the photoexcited carbon nitride nanosheet can transfer to UiO-66, which can substantially suppress electron–hole pair recombination in the carbon nitride nanosheet, as well as supply long-lived electrons for the reduction of CO_2 molecules that are adsorbed in UiO-66. As a result, the UiO-66/carbon nitride nanosheet heterogeneous photocatalyst exhibits a much higher photocatalytic activity for the CO_2 conversion than that of bare carbon nitride nanosheets. We believe this self-assembly method can be extended to other carbon nitride nanosheet loaded materials.

1. Introduction

The production of chemical fuels using CO_2 as a carbon source has been regarded as an ideal solution to the problems with energy shortage and global warming.[1] Photocatalytic reduction of CO_2 through artificial photosynthesis is of significant interest as it offers the potential to produce valuable hydrocarbon fuels to meet increasing energy demands while also mitigating the rising CO_2 levels.[2] A great deal of effort has been devoted to exploring photocatalysts that are capable of reducing CO_2. In photocatalytic processes, the photocatalyst is excited by light of an energy level that is greater than the photocatalyst's bandgap to generate electron–hole pairs, which are separated and then transferred to the catalytically active sites for redox reactions.[3] The CO_2 conversion efficiency of the photocatalyst essentially relies on the lifetime of the photogenerated electron–hole pairs, the separation efficiency of the photoinduced charge carriers, the CO_2 molecule adsorption, and the activation.[4] In particular, increasing the CO_2 adsorption ability of photocatalysts has been proven to be an effective strategy to improve the CO_2 conversion efficiency, as the electron transfer from the catalytically active sites of the photocatalysts to the CO_2 molecules largely relies on their intimate and stable binding. Therefore, in order to improve photocatalytic CO_2 conversion, an ideal solution is to incorporate a photocatalyst into a CO_2 sorbent material. For instance, zeolites or mesoporous materials modified with TiO_2 photocatalysts have been widely studied for photocatalytic CO_2 reduction, and showed improved CO_2 adsorption ability and a higher photocatalytic CO_2 conversion efficiency compared to bare TiO_2.[5,6] The role of the zeolite material can be summed up by the so-called "catch and release effect of CO_2", i.e., capture of CO_2 molecules, followed by the efficient diffusion of the CO_2 molecules to the TiO_2 active sites.[7] However, the improvements in photocatalytic activity are quite limited, mainly due to the fact that zeolite itself cannot provide the active sites for photocatalytic CO_2 reduction and the photocatalytic efficiency therefore largely depends on the efficient diffusion of the CO_2 molecules from the zeolite to the active sites of the photocatalysts.

Metal-organic frameworks (MOFs) are a class of porous solid materials composed of metal-containing clusters and organic building blocks, which have demonstrated wide applications in drug delivery, catalysis, gas capture, and separation.[8–12] UiO-66, a zirconium-based MOF, has attracted intense research interest because of its higher chemical stability and thermostability compared to other types of MOFs.[13] UiO-66 has been considered to be a promising material for CO_2 capture and storage.[14] Moreover, recent studies have proven that UiO-66 exhibits semiconductor behavior, which can facilitate charge transfer or harvest solar light directly for photocatalytic reactions.[15–18]

L. Shi, Prof. J. Ye
Graduate School of Chemical Sciences and Engineering
Hokkaido University
Sapporo 060–0814, Japan
E-mail: jinhua.ye@nims.go.jp
L. Shi, Dr. T. Wang, Dr. H. Zhang, Dr. K. Chang, Prof. J. Ye
Environmental Remediation Materials Unit and International Center for Materials Nanoarchitectonics (WPI-MANA)
National Institute for Materials Science (NIMS)
1–1 Namiki, Tsukuba, Ibaraki 305–0044, Japan
Dr. T. Wang
Jiangsu Key Laboratory of Materials and Technology for Energy Conversion
College of Materials Science and Technology
Nanjing University of Aeronautics and Astronautics
Nanjing 210016, P. R. China
Prof. J. Ye
TU-NIMS Joint Research Center
School of Materials Science and Engineering
Tianjin University
92 Weijin Road, Nankai District, Tianjin, P. R. China
Prof. J. Ye
Collaborative Innovation Center of Chemical Science and Engineering
Tianjin 300072, P. R. China

DOI: 10.1002/adfm.201502253

UiO-66 has also been demonstrated to have active sites for the photocatalytic reduction of CO_2.[19] Nevertheless, the relatively wide bandgap of UiO-66 may limit its optical adsorption in the visible-light region. To prepare UiO-66 based visible-light active photocatalysts, an ideal solution would be to incorporate UiO-66 together with a visible-light active photosensitizer, such as narrow bandgap semiconductors, to form a heterogeneous photocatalyst. The key to this type of heterogeneous photocatalyst is whether the photoexcited electron from the photosensitizer can be efficiently transferred to UiO-66.

Graphitic carbon nitride (CN), a metal-free and visible-light active photocatalyst, has attracted increasing attention and been reported to possess the photocatalytic performance for water splitting, organic degradation and transformation, and it has also been explored for the photocatalytic conversion of CO_2.[20–24] However, the efficiency of bulk carbon nitride (bulk CN) is far from satisfactory, mainly due to the fast recombination of the photogenerated electron–hole pairs. The exfoliation of bulk CN to 2D atomic carbon nitride nanosheet (CNNS) has been actively pursued to improve the photocatalytic activity, because of the synergistic effect of the increased bandgap, enhanced electron-transport properties, and prolonged lifetime.[25–27] However, further improvement of the efficiency for photocatalytic CO_2 reduction is limited, mainly due to the fact that the efficient capture of CO_2 molecules by carbon nitride remains a challenge. The integration of carbon nitride with UiO-66 may offer an attractive way to improve the efficiency of photocatalytic CO_2 reduction. The colloidal suspension of CNNS with highly flexible and soft nature, as well as negatively charged surfaces, made it possible for the self-assembly of CNNS based heterogeneous photocatalysts with desired separation of the photogenerated charge carriers.[28,29]

Herein, we report a facile self-assembly synthesis of a UiO-66/CNNS heterogeneous photocatalyst through the electrostatic reaction between the negatively charged nanosized CNNS and positively charged UiO-66. To the best of our knowledge, this is the first time that a MOF/CNNS hybrid structure is prepared by electrostatic self-assembly. In addition, we also prepared a UiO-66/bulk CN heterogeneous photocatalyst via the same method. We investigated the photocatalytic CO_2 reduction of the UiO-66/CNNS hybrid structure, CNNS, UiO-66/bulk CN hybrid structure, and bulk CN. It is shown that CNNS has a higher activity than bulk CN, and the formation of a hybrid structure further improves the photocatalytic CO_2 conversion efficiency. These hybrid structures exhibit a large surface area and strong CO_2 capture ability. We demonstrate that the electrons from photoexcited CNNS or bulk CN can transfer to UiO-66, which can substantially suppress electron–hole pair recombination in the CNNS or bulk CN, as well as supply long-lived electrons for the reduction of CO_2 molecules adsorbed in UiO-66.

2. Results and Discussion

2.1. Characterization of Photocatalysts

The formation of the UiO-66/CNNS hybrid structure involved a two-step process, as explained in the Experimental Section and shown in **Figure 1**a. Firstly, CNNS were obtained by a liquid exfoliation route from bulk CN in water. Secondly, a predefined mass ratio of the as-prepared CNNS and UiO-66 were dispersed in water under vigorous stirring, and then these CNNS spontaneously coated on UiO-66 through an electrostatic self-assembly process. Figure 1b shows the transmission electron microscopy (TEM) images of the exfoliated CNNS. It can be seen that the as-obtained CNNSs are freestanding with a diameter of 15 ± 5 nm. The high-resolution TEM (HRTEM) image (Figure 1b, inset) shows that the edge of the CNNS is nearly transparent, which indicates their ultrathin thickness. Atomic force microscopy (AFM) was performed to gain more information about the morphology and thickness of the CNNS. A typical AFM image in Figure 1c,d shows that the thickness of a randomly measured nanosheet is about 3.6 nm, indicating that the exfoliated CNNS only consists of ten C-N layers. The crystal and electronic structures of the CNNS were studied by recording their X-ray diffraction (XRD) patterns, optical absorption, and photoluminescence (PL) spectra and comparing them with those of bulk CN (**Figure 2**a–c). As presented in Figure 2a, the CNNS shows two peaks at 13.1° (100) and 27.4° (002), which is consistent with those of bulk CN, indicating that CNNS basically exhibit the same crystal structure as bulk CN. Compared to bulk CN, the peak corresponding to the (002) in the CNNS was slightly shifted from 27.7° to 27.4°, which can be attributed to the loosely layered structure of CNNS swelled by water. Moreover, in the case of CNNS, the peak at 13.1° became less pronounced, which can be ascribed to the decreased planar size of the layers during exfoliation from bulk CN.[25,26] The UV-vis absorption spectra in Figure 2b shows that the intrinsic absorption edge of the CNNS displays an obvious blue shift compared with that of bulk CN, and the bandgap of the CNNS increased to 2.78 eV compared to 2.63 eV for bulk CN. Moreover, the PL spectrum shows that the emission peak of CNNS exhibits a blue shift of 21 nm in comparison with that of bulk CN (Figure 2c). The reason for the larger bandgap and the blue shift of the PL spectra in CNNS can be attributed to the quantum-confinement effect with the conduction and valence band edges shift in opposite directions.[28]

Valence-band X-ray photoelectron spectroscopy (VB-XPS) was carried out to investigate the VB top level of bulk CN and CNNS. As shown in Figure S1 in the Supporting Information, the energy level valence-band maximum (VBM) of bulk CN and CNNS are 1.62 eV and 1.68 eV, respectively. Therefore, in our case, the CNNS has a higher bandgap by 0.15 eV as a result of a lower valence-band edge by 0.06 eV and a higher conduction band edge by 0.09 eV compared to bulk CN. According to the literature, the position of the conduction band edge for bulk CN is located at −1.3 V vs. the normal hydrogen electrode (NHE) at pH 7.[30] Therefore, it can be established that the position of the conduction band edge for CNNS is located at −1.39 V (vs. NHE, pH 7).

The as-prepared CNNS was coated on the surface of UiO-66, which was confirmed by TEM images of the UiO-66 MOF crystal and the UiO-66/CNNS composite. The as-obtained UiO-66 MOF compound shows well-defined nanocrystals with a narrow size distribution (Figure 1e,f). The HRTEM image (Figure 1f, inset) indicates that the surface of the UiO-66 crystal is rough, which is beneficial for loading the CNNS. Figure 1g shows the TEM image of the UiO-66/CNNS hybrid structure, indicating that the CNNS were well coated on the surface of UiO-66 without much aggregation. Importantly, the HRTEM image

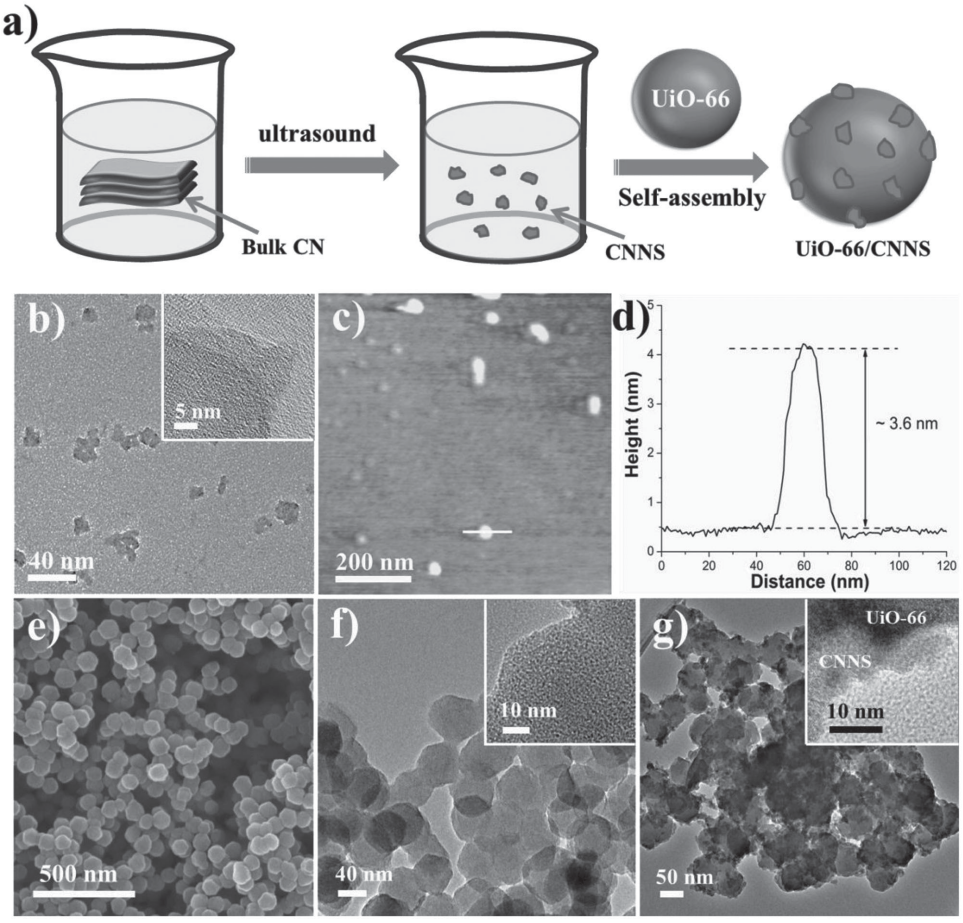

Figure 1. a) Schematic illustration of the preparation of the UiO-66/CNNS heterogeneous photocatalyst. b) TEM and HRTEM images of CNNS; c,d) AFM and corresponding height images of CNNS. e,f) SEM, TEM, and HRTEM images of UiO-66. g) TEM and HRTEM images of UiO-66/CNNS. The CNNS content in UiO-66/CNNS composite is 10 wt%.

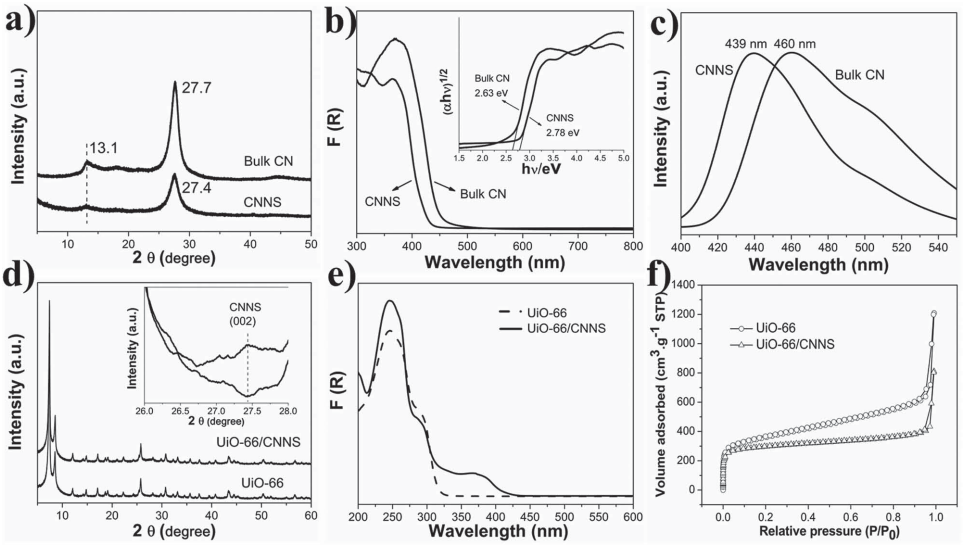

Figure 2. a–c) XRD patterns, diffuse-reflectance UV-vis spectrum, and PL spectra of bulk CN and CNNS. d–f) XRD patterns, diffuse-reflectance UV-vis spectrum, and N_2 adsorption-desorption isotherms of UiO-66 and UiO-66/CNNS. The CNNS content in the UiO-66/CNNS composite was 10 wt%.

(Figure 1g, inset) shows a distinguished and coherent interface between the UiO-66 crystal and the CNNS, indicating that nanojunctions might be formed in the UiO-66/CNNS hybrid structure, which could result in efficient electron transfer within the hybrid structure. Elemental mapping analysis (Figure S2, Supporting Information) clearly shows the well-defined spatial distribution of the Zr and N elements, which confirms that the CNNS were uniformly coated on the UiO-66. In order to investigate the self-assembly mechanism between CNNS and UiO-66, zeta potential measurements were carried out. The dispersed CNNS in water is negatively charged, with a zeta potential of about –35.91 mV, whereas UiO-66 shows a zeta potential value of +7.71 mV, indicating its positively charged surface. The zeta potential measurements results indicate that the hybrid structure between CNNS and UiO-66 was formed through electrostatic self-assembly process. The crystallographic structure of the products was determined by XRD. As shown in Figure 2d, the characteristic peaks of UiO-66 can clearly be identified in the spectrum of the UiO-66/CNNS composite, suggesting that the crystal phase structure of UiO-66 is retained after being coated by CNNS.[15–18] The enlarged XRD pattern in Figure 2d confirms that the sample is a hybrid structure between UiO-66 and CNNS. The optical absorption of the UiO-66 MOF compound and the UiO-66/CNNS hybrid structure was measured by UV-vis absorption. As illustrated in Figure 2e, UiO-66 can only absorb UV-light with wavelengths that are shorter than 350 nm, whereas the UiO-66/CNNS hybrid structure has an absorption edge at about 440 nm, which is similar to that of CNNS. The enhancement of light absorption in the visible region further confirms the formation of a hybrid structure between UiO-66 and CNNS. Figure 2f shows the N_2 adsorption–desorption isotherms for the UiO-66 MOF compound and the UiO-66/CNNS hybrid structure, respectively. The bare UiO-66 MOF sample attained a Langmuir surface area of 1610.5 m^2 g^{-1}, whereas the UiO-66/CNNS hybrid structure showed a relatively low surface area (1315.3 m^2 g^{-1}). The decrease in surface area after CNNS coating can be explained by the fact that the CNNS account for 10% of the total weight and exhibit a much smaller surface area (Figure S3, Supporting Information). The bulk CN dispersed in water was also negatively charged, with a measured zeta potential of –24.27 mV, thus a UiO-66/bulk CN composite could also be formed through electrostatic self-assembly. The XRD patterns and UV-vis absorption spectra demonstrate that a hybrid composite consisting of bulk CN and UiO-66 was formed successfully (Figure S4, Supporting Information). Further information about the microstructure of the UiO-66/bulk CN composite was obtained from TEM images. As shown in Figure S5 in the Supporting Information, the UiO-66 crystals are coated by bulk CN, thereby forming nanojunctions in the UiO-66/bulk CN composite. The Langmuir surface area of the UiO-66/bulk CN composite was 1340.9 m^2 g^{-1} (Figure S6, Supporting Information), which is close to that of the UiO-66/CNNS composites.

2.2. CO_2 Adsorption and Electron Transfer Behavior

Figure 3a shows the CO_2-adsorption behavior of the samples at room temperature. It can be seen that the maximum CO_2

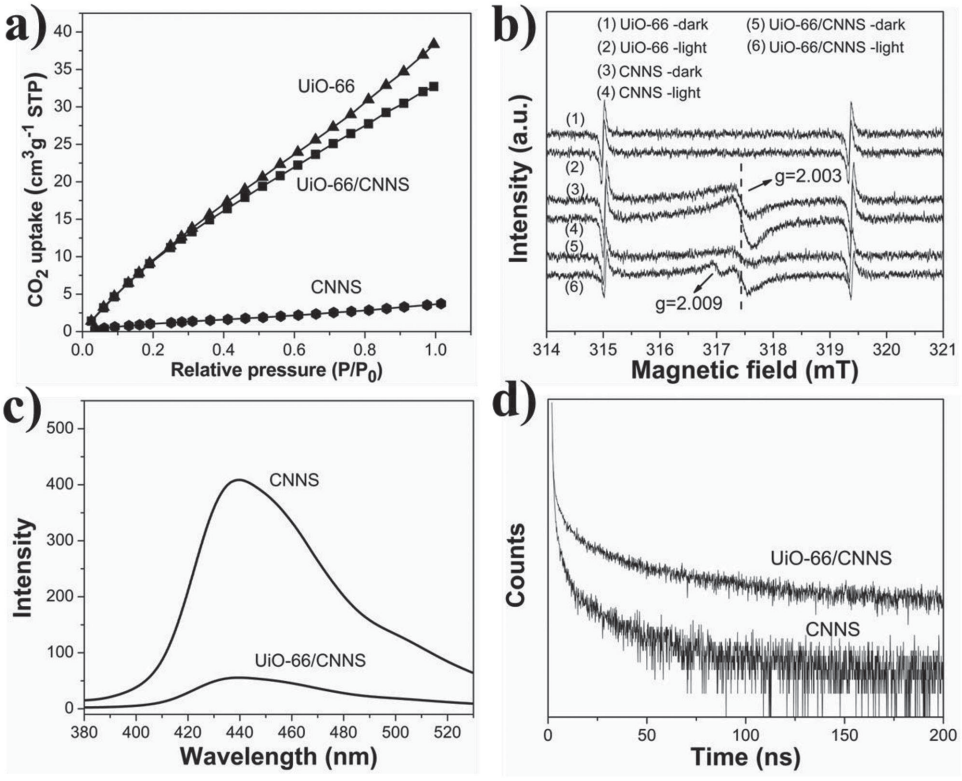

Figure 3. a,b) CO_2 adsorption isotherms and ESR spectra of UiO-66, CNNS, and UiO-66/CNNS. c,d) PL spectra and decay curve of CNNS and UiO-66/CNNS. The CNNS content in the UiO-66/CNNS composite was 10 wt%.

uptake for the UiO-66 MOF, UiO-66/CNNS composite, and CNNS samples were 38.4 $cm^3\ g^{-1}$, 32.7 $cm^3\ g^{-1}$, and 3.7 $cm^3\ g^{-1}$, respectively. The comparison of the CO_2-adsorption behavior of the above three samples indicates that the UiO-66/CNNS composite showed a superior CO_2 uptake ability than that of CNNS because of the high adsorption capability of UiO-66 MOF. This suggests that the CNNS coating layers are finely dispersed on the surface of UiO-66, without significant pore blockage of the UiO-66, and that the CO_2 molecules can be adsorbed on the microporous UiO-66 cores. The CO_2-adsorption behavior of the UiO-66/bulk CN composite and bulk CN were also investigated and are shown in Figure S7 (Supporting Information). The maximum CO_2 uptake for the UiO-66/bulk CN composite was 35.9 $cm^3\ g^{-1}$, which is much higher than that of bulk CN (1.1 $cm^3\ g^{-1}$).

It is important to note that UiO-66 has been proven to be a semiconductor material with a conduction band-edge potential of −0.6 V (vs. NHE, pH 7), which is much lower than that of CNNS.[18,31] Therefore, the nanojunction formed between UiO-66 and CNNS could result in efficient electron transfer within the hybrid structure and better separation of the photoinduced charge carriers. Figure 3b shows the electron spin resonance (ESR) spectra of UiO-66, CNNS, and the UiO-66/CNNS composite measured at room temperature under air atmosphere. For CNNS, a *g* value of 2.003 was observed, which could be ascribed to the unpaired electrons on the carbon atoms of the aromatic rings within the π-bonded nanosized clusters.[32] The intensity of this ESR signal increased under visible light illumination, which provides a clue about the promoted photogeneration of radical pairs in the CNNS.[32] However, in the case of the UiO-66/CNNS composite, an enhanced *g* value of 2.003 was found as well as a new ESR signal with a *g* value of 2.009. According to the literature, the new signal can be attributed to $O_2^{-\bullet}$ species formed from photogenerated electrons adsorbed on the UiO-66 matrix.[17] In contrast, when pristine UiO-66 was irradiated with visible light, the above ESR signal was not detected, due to the fact that UiO-66 has a large bandgap that cannot be excited under visible light. The ESR results show that CNNS can act as a photosensitizer to harvest visible light and the electrons generated from the conduction band of CNNS transfer to UiO-66, and consequently transfer to the adsorbed oxygen molecules in the cage of UiO-66. Further insight into the electron transfer behavior was revealed by PL-quenching and fluorescence-lifetime experiments (Figure 3c,d). These results show that, in the presence of UiO-66, there is significant quenching of the PL intensity and an increase in the fluorescence lifetime, indicating that the recombination of photoexcited electron–hole pairs is significantly suppressed and the separation of electron–hole pairs is efficiently improved. The decay curves could be fitted well with a tri-exponential function and the calculated average lifetime values were 481.4 ns for CNNS and 846.3 ns for the UiO-66/CNNS composite. The longer lifetime attained by the UiO-66/CNNS composite could be ascribed to electron transfer from the conduction band of CNNS to UiO-66, after which these electrons are localized in UiO-66. The electron transfer behavior in the UiO-66/bulk CN composite was also confirmed by the quenching of the PL intensity and the increase in fluorescence lifetime (Figure S8, Supporting Information).

2.3. Evaluation of Photocatalytic Activity

The photocatalytic properties of all samples were evaluated by investigating the photocatalytic reduction of CO_2, which was carried out in a reaction system using triethanolamine (TEOA) as the electron donor, under mild reaction conditions (Figure S9, Supporting Information). Firstly, the photocatalytic activity for CO_2 reduction of UiO-66/CNNS composites with different CNNS contents was investigated. After the photocatalytic reaction, neither H_2 nor hydrocarbon gases were detected, and CO was the main gas product from the CO_2 reduction (Figure S10, Supporting Information). The photocatalytic CO evolution rates are summarized in Table S1 in the Supporting Information. It should be noted that the CO evolution rate increased with increasing CNNS content up to about 10%, beyond which it decreased again. Therefore, we further investigated the CO evolution activity of hybrid structures containing 10 wt% carbon nitride. **Figure 4**a shows the time-dependent conversion yields of CO_2 into CO using our samples as photocatalysts under light irradiation. The generation of CO increased almost linearly with irradiation time and it is clear that CNNS exhibits a higher efficiency for CO_2 conversion than that of bulk CN. Furthermore, we found that the CO yield increased after introduction of UiO-66. The UiO-66/CNNS composite showed the highest CO evolution rate and it attained a CO yield of 59.4 μmol g_{CN}^{-1} under light illumination for 6 hours, which is over three times than that of CNNS (17.1 μmol g_{CN}^{-1}). The CO evolution yield of the UiO-66/bulk CN composite reached 19.3 μmol g_{CN}^{-1} after 6 hours, which is 1.6-fold larger than that of bulk CN. This experiment demonstrates the superiority of the hybrid structure in photocatalytic CO_2 conversion. When the experiment was conducted in the absence of photocatalysts or light illumination, no detectable CO was formed in the reaction system. To further validate the source of the generated CO product, an isotopic experiment using $^{13}CO_2$ as substrate was performed under

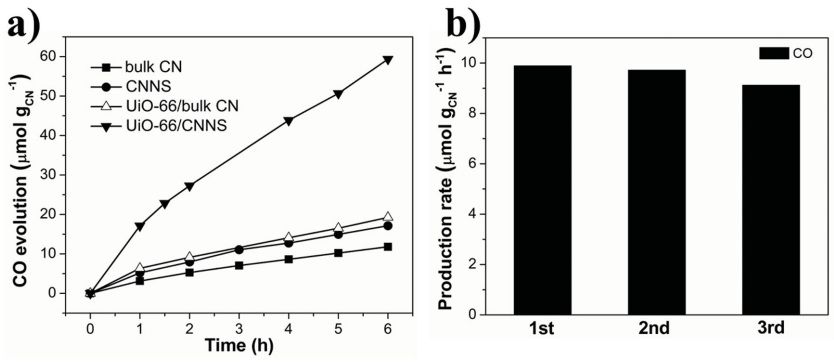

Figure 4. a) Time course of CO evolution over bulk CN, CNNS, UiO-66/bulk CN, and UiO-66/CNNS photocatalysts. b) Production yield of CO over UiO-66/CNNS photocatalyst to measure reproducibility by cycling tests. For the hybrid structures, the carbon nitride content was 10 wt%.

identical photocatalytic reaction conditions, and the products were analyzed by gas chromatography and mass spectra. As shown in Figure S11 (Supporting Information), the peak at m/Z 29 could be assigned to ^{13}CO, indicating that the carbon source of CO did indeed originate from the used CO_2. The stability and reusability of the UiO-66/CNNS composite photocatalyst were also investigated. After reaction, the UiO-66/CNNS composite was removed from the reaction system and characterized by XRD and morphology analyses (Figure S12 and S13, respectively, Supporting Information). The results show that the UiO-66/CNNS composite has a strong resistance to structural and morphological changes, which reflects its stability during the photocatalytic CO_2 conversion reaction. The reusability of the photocatalyst was studied by collecting and reusing the photocatalyst for three times. As shown in Figure 4b, the UiO-66/CNNS composite photocatalyst exhibits a fairly reproducible photocatalytic activity for all three cycles.

2.4. Clarification of the Mechanism

The above information clearly shows the photocatalytic performance of CN for CO_2 reduction and it also demonstrates the improvement in photocatalytic activity when using a hybrid structure formed by the integration of a Zr-based MOF structured as UiO-66 with CN. We now try to understand the mechanisms behind the function of the hybrid structure. It is well known that the band structure, the lifetime of the photogenerated electron–hole pairs, the separation efficiency of the photoinduced charge carriers, the CO_2 adsorption, and activation are crucial factors that influence the photocatalytic CO_2 conversion efficiency.[4] It is important to note that the position of the conduction band for bulk CN is –1.3 V (vs. NHE, pH 7), which is negative enough to reach the corresponding reduction potential of CO_2 to produce CO ($CO_2 + 2H^+ + 2e^- \rightarrow CO + H_2O$, –0.48 V vs. NHE at pH 7).[4] Both the theoretical prediction and experimental results have proven that the bandgap enlargement of 0.15 eV in exfoliated CNNS could be ascribed to a shift in both the conduction band and valence band in opposite directions, and thus the CNNS shows a higher conduction band edge and a lower valence band edge compared to those of bulk CN, which enhances the photoredox ability.[28] The enhancement of the photoredox ability in CNNS is responsible for its higher photocatalytic CO_2 reduction performance with respect to bulk CN. Moreover, as is shown in **Table 1**, the CO_2 adsorption ability and lifetime of CNNS are higher than those of bulk CN, which also explains their higher photocatalytic CO_2 reduction performance. The photocatalytic CO_2 reduction performance can be further improved through the introduction of UiO-66. It was observed that UiO-66 itself did not show any detectable photocatalytic activity under visible light irradiation, because of its large bandgap that can only adsorb UV light (Figure 2e, Table 1). Therefore, the enhancement of the photocatalytic activity for the hybrid structure can be attributed to the synergistic effects of enhanced CO_2 adsorption, separation efficiency of photoinduced charge carriers, and prolonged lifetime of photogenerated electron–hole pairs, as evidenced above.

We did, however, observe a significant difference in the activity improvement in the photocatalytic CO_2 reduction for the UiO-66/CNNS and UiO-66/bulk CN composites compared to pristine CNNS and bulk CN, respectively. The CO evolution rate of the UiO-66/CNNS composite shows a 3.4-fold improvement compared to that of CNNS, whereas the UiO-66/bulk CN composite shows a 1.6-fold improvement compared to bulk CN. Taking into account that the UiO-66/CNNS composite and the UiO-66/bulk CN composite have a similar surface area and CO_2 adsorption ability, the significant difference in the activity enhancement for the two composites can be ascribed to the difference in lifetime improvement. As shown in Table 1, the lifetime of the UiO-66/CNNS composite shows a 75.8% improvement compared with CNNS and reaches 846.3 ns, whereas the UiO-66/bulk CN only shows a 64.7% improvement compared to bulk CN and reaches 690.4 ns. This suggests that the designed UiO-66/CNNS hybrid system is much more robust for improving the efficiency of electron–hole separation, and this can be explained by three main reasons. First of all, compared to bulk CN, CNNS has a bandgap that is larger by 0.15 eV as a result of a higher conduction band and lower valence band, which means that CNNS can provide a stronger driving force for the transfer of electrons to UiO-66 as a result of the larger energy-level difference between the conduction band edge of CNNS and UiO-66. Secondly, it is well known that the electron-transfer process in our hybrid structure involves two steps: photoexcited electrons in the CNNS or bulk CN migrate to the surface of CNNS or bulk CN, and subsequently transfer to UiO-66. Compared to bulk CN, the unique nanosheet structure of CNNS can shorten the electron-transport distance between UiO-66 and the excitation center in the CNNS, thus facilitating efficient electron transfer and reducing the bulk recombination probability of charge carriers in CNNS. In addition, CNNS have a flexible structure, soft nature, and a more negatively charged surface, which are more easily adsorbed on the UiO-66 surface in a uniform way compared to bulk CN, and this will increase the binding force between CNNS and UiO-66. It is thereby easier for photogenerated electrons from CNNS to transfer to UiO-66 than from bulk CN. The electrons that are localized in UiO-66 are sufficiently long-lived, resulting in a higher electron density in the UiO-66/CNNS composite, a feature that is also beneficial for the activation of CO_2 that is adsorbed in UiO-66, as the production of CO is a multi-electron process.[33]

On the basis of the above discussion, a tentative mechanism for the photocatalytic CO_2 reduction over the UiO-66/CNNS composite is proposed, as shown in **Figure 5**. Upon

Table 1. Comparison of the properties and photocatalytic activity of different samples. For the hybrid-structure photocatalysts, the carbon nitride content was 10 wt%. The photocatalytic reaction was conducted for 6 hours. Light source: 400 nm < λ < 800 nm

Sample	Surface area [$m^2\ g^{-1}$]	Maximum CO_2 uptake [$cm^3\ g^{-1}$]	Average lifetime [ns]	CO evolution rate [$\mu mol\ g_{CN}^{-1}\ h^{-1}$]
UiO-66	1610.5[a]	38.4	–	n.d.[c]
Bulk CN	48.2[b]	1.1	419.3	2.0
UiO-66/bulk CN	1340.9[a]	35.9	690.4	3.2
CNNS	108.7[b]	3.7	481.4	2.9
UiO-66/CNSS	1315.3[a]	32.7	846.3	9.9

[a]Langmuir surface area; [b]BET surface area; [c]Not detectable.

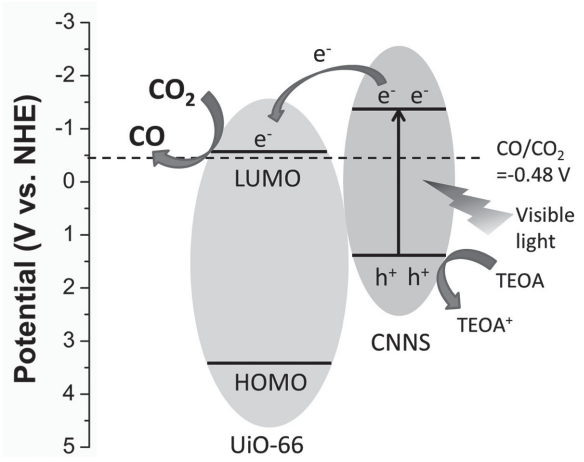

Figure 5. Proposed mechanism of photocatalytic reduction of CO_2 by the UiO-66/CNNS heterogeneous photocatalyst under visible light irradiation.

visible light irradiation electrons are promoted from the valence band of CNNS to its corresponding conduction band. Those photogenerated electrons migrate to the surface of CNNS and then transfer to UiO-66 across the interface between CNNS and UiO-66. The electrons in UiO-66 can reduce the adsorbed CO_2 to CO, and simultaneously, the holes that remained within the valence band of CNNS are consumed by TEOA, which acts as an electron donor.

3. Conclusions

We have demonstrated a facile method to synthesize a UiO-66/CNNS hybrid structure by electrostatic self-assembly of negatively charged CNNS with positively charged UiO-66. The designed hybrid structure possessed not only a large surface area and strong CO_2 adsorption ability, but also improved electron separation and prolonged lifetime of the charge carriers as a result of efficient electron transfer across the interface between CNNS and UiO-66. As a result, the UiO-66/CNNS composite photocatalyst exhibited a much higher photocatalytic activity for CO_2 conversion compared to bare CNNS under mild reaction conditions. Similarly, a UiO-66/bulk CN hybrid structure was also prepared and showed enhanced activity for the photocatalytic reduction of CO_2 compared to that of bulk CN, which is due to the strong CO_2 adsorption ability of UiO-66 and its efficient charge transfer. It is anticipated that this work will provide a strategy to design more active photocatalysts for CO_2 conversion, as well as open up opportunities to develop various MOF-based photocatalysts for gaseous reactions.

4. Experimental Section

4.1. Materials

Melamine, *N*,*N*-dimethylformamide (DMF), 1,4-benzenedicarboxylic acid (BDC), zirconium chloride ($ZrCl_4$), acetonitrile (MeCN), and triethanolamine (TEOA) were purchased from Wako Co. All reagents were analytical grade and used without further purification. The deionized water (18.2 MΩ) that was used throughout all experiments was produced using a Millipore Direct-Q System.

4.2. Preparation of the Photocatalysts

Bulk CN was prepared by heating melamine in a crucible to 550 °C for 4 hours under air. Nanosized CNNS were obtained by liquid exfoliating of as-prepared bulk CN in water. In brief, 0.1 g bulk CN powder was dispersed in 100 mL of H_2O, then ultrasonicated in a water bath for 5 h using a Branson-250 sonicator (Japan) with an output power of 48 W. After this process, the suspension was left to stand overnight and then centrifuged at 9000 rpm for 10 min to remove any residual non-exfoliated bulk CN and large-sized CNNS. The nanosized CNNS were collected by evaporating the supernatant. UiO-66 was synthesized from a mixture of $ZrCl_4$, BDC, and DMF with a molar ratio of 1:1:650, then the mixture was heated at 120 °C for 48 hours. The resulting white UiO-66 products were collected by centrifugation and washed with DMF and water several times, and then activated at 200 °C for 12 hours under vacuum to remove any organic solvent. The UiO-66/CNNS composite was prepared by mixing UiO-66 and nanosized CNNS with known mass ratio in water. The suspension was ultrasonicated for 10 min and then stirred for 24 hours. After evaporation of the water, the powder was obtained after drying at 100 °C under vacuum. The UiO-66/bulk CN composite was prepared in a similar way expect that bulk CN was used instead of CNNS.

4.3. Characterization

The prepared samples were characterized by powder XRD on an X-ray diffractometer (Rint 2000, Altima III, Rigaku Co. Japan) using a Cu Kα source. UV-vis diffuse reflectance spectra were measured on a UV-visible spectrophotometer (Shimadzu, UV-2600) with $BaSO_4$ as the reflectance standard reference. The morphology and structure of the samples were examined by scanning electron microscopy (SEM, S4800, Hitachi Co., Japan) and transmission electron microscopy (TEM, 2100F, JEOL Co., Japan). CO_2 adsorption isotherms were measured at room temperature using a BEL SORP-mini II (BEL Japan INC., Japan). Nitrogen adsorption–desorption isotherms were recorded using nitrogen physisorption (Autosorb-iQ_2-MP; Quantachrome Corp., U.S.A.). The thickness of the CNNS was measured by dynamic force microscopy (DFM) (Nanocute H, Japan). The valence bands of the samples were determined using X-ray photoelectron spectroscopy (XPS, PHI Quantera SXM, ULVAC-PHI Inc., Japan). The zeta potential of all samples was recorded on an ELSZ-2000 (Otsuta Electronics), and the solvent was pure water. All zeta-potential measurements were repeated three times and the average values were used. The PL spectra were recorded on a JASCO FP-6500 spectrofluorometer. The decay time was measured by a fluorescent spectrophotometer (Horiba Jobin Yvon, Fluorolog-3) with a nano-LED lamp (370 nm) as the excitation source (Horiba Jobin Yvon). The experimental details of the decay-time measurements are described below: the powder sample was transferred to a substrate and the decay-time measurements were conducted directly on a powder sample with an excitation light wavelength of 370 nm. Electron spin resonance (ESR) characterizations were carried out using a JEOL JES-FA-200 at room temperature in air.

4.4. Photocatalytic Experiments

The photocatalytic activities of all samples were carried out in a batch-type reaction system with a total volume of about 330 mL. The setup of the photocatalytic system is illustrated in Figure S9 in the Supporting Information. The sample was uniformly dispersed on a porous quartzose film in the reaction cell, and 5 mL of solution (MeCN/TEOA = 4:1) was injected into the cell. After complete evacuation of

the reaction system (no O_2 or N_2 could be detected), 80 kPa of pure CO_2 gas was injected into the airtight system. A 300 W xenon arc lamp with a UV-cut filter, to remove light with wavelengths lower than 400 nm, and an IR-cut filter to remove wavelengths longer than 800 nm light filters (400 nm < λ < 800 nm) was used as the light source. In the measurements, known amounts of powdered samples were used (keeping the visible light photoactive carbon nitride material at the same weight). Prior to testing, the catalysts were degassed at 200 °C for 12 hours under vacuum to remove any possible organic contaminants. The gas products were measured using gas chromatography (GC-14B, Shimadzu Co., Japan). The isotope of ^{13}C was analyzed using gas chromatography-mass spectrometry (JEOL-GCQMS, JMS-K9 and 6890N Network GC system, Agilent Technologies).

Supporting Information

Supporting Information is available from the Wiley Online Library or from the author.

Acknowledgments

This work was partially supported by the World Premier International Research Center Initiative on Materials Nanoarchitectonics (MANA), MEXT (Japan), National Basic Research Program of China (973 Program, 2014CB239301), and the MITSUBISHI Foundation. We are grateful to Dr. Xiaojun Wang for her help with the measurements of the PL lifetime and discussion of the results.

Received: June 2, 2015
Revised: June 28, 2015
Published online: July 27, 2015

[1] S. C. Roy, O. K. Varghese, M. Paulose, C. A. Grimes, *ACS Nano* **2010**, *4*, 1259.
[2] X. Zhang, F. Han, B. Shi, S. Farsinezhad, G. P. Dechaine, K. Shankar, *Angew. Chem. Int. Ed.* **2012**, *51*, 11778.
[3] H. Tong, S. Ouyang, Y. Bi, N. Umezawa, M. Oshikiri, J. Ye, *Adv. Mater.* **2012**, *24*, 229.
[4] W. Tu, Y. Zhou, Z. Zou, *Adv. Mater.* **2014**, *26*, 4607.
[5] H. Yamashita, Y. Fujii, Y. Ichihashi, S. G. Zhang, K. Ikeue, D. R. Park, K. Koyano, T. Tatsumi, M. Anpo, *Catal. Today* **1998**, *45*, 221.
[6] M. Anpo, H. Yamashita, K. Ikeue, Y. Fujii, S. G. Zhang, Y. Ichihashi, D. R. Park, Y. Suzuki, K. Koyano, T. Tatsumi, *Catal. Today* **1998**, *44*, 327.
[7] M. Takeuchi, S. Sakai, A. Ebrahimi, M. Matsuoka, M. Anpo, *Top. Catal.* **2009**, *52*, 1651.
[8] P. Horcajada, C. Serre, G. Maurin, N. A. Ramsahye, F. Balas, M. V. Regí, M. Sebban, F. Taulelle, G. Férey, *J. Am. Chem. Soc.* **2008**, *130*, 6774.
[9] J.-L. Wang, C. Wang, W. Lin, *ACS Catal.* **2012**, *2*, 2630.
[10] L. Shi, T. Wang, H. Zhang, K. Chang, X. Meng, H. Liu, J. Ye, *Adv. Sci.* **2015**, *2*, 1500006.
[11] T. M. McDonald, W. R. Lee, J. A. Mason, B. M. Wiers, C. S. Hong, J. R. Long, *J. Am. Chem. Soc.* **2012**, *134*, 7056.
[12] Y. Mao, L. Shi, H. Huang, W. Cao, J. Li, L. Sun, X. Jin, X. Peng, *Chem. Commun.* **2013**, *49*, 5666.
[13] J. H. Cavka, S. Jakobsen, U. Olsbye, N. Guillou, C. Lamberti, S. Bordiga, K. P. Lillerud, *J. Am. Chem. Soc.* **2008**, *130*, 13850.
[14] C. H. Lau, R. Babarao, M. R. Hill, *Chem. Commun.* **2013**, *49*, 3634.
[15] L. Shen, S. Liang, W. Wu, R. Liang, L. Wu, *J. Mater. Chem. A* **2013**, *1*, 11473.
[16] L. Shen, W. Wu, R. Liang, R. Lin, L. Wu, *Nanoscale* **2013**, *5*, 9374.
[17] J. Long, S. Wang, Z. Ding, S. Wang, Y. Zhou, L. Huang, X. Wang, *Chem. Commun.* **2012**, *48*, 11656.
[18] Z. Sha, J. Sun, H. S. O. Chan, S. Jaenicke, J. Wu, *RSC Adv.* **2014**, *4*, 64977.
[19] D. Sun, Y. Fu, W. Liu, L. Ye, D. Wang, L. Yang, X. Fu, Z. Li, *Chem. Eur. J.* **2013**, *19*, 14279.
[20] X. Wang, K. Maeda, A. Thomas, K. Takanabe, G. Xin, J. M. Carlsson, K. Domen, M. Antonietti, *Nat. Mater.* **2009**, *18*, 76.
[21] S. C. Yan, Z. S. Li, Z. G. Zou, *Langmuir* **2010**, *26*, 3894.
[22] X. Chen, J. Zhang, X. Fu, M. Antonietti, X. Wang, *J. Am. Chem. Soc.* **2009**, *131*, 11658.
[23] Z. Lin, X. Wang, *Angew. Chem. Int. Ed.* **2013**, *52*, 1735.
[24] P. Niu, Y. Yang, J. C. Yu, G. Liu, H.-M. Cheng, *Chem. Commun.* **2014**, *50*, 10837.
[25] S. Yang, Y. Gong, J. Zhang, L. Zhan, L. Ma, Z. Fang, R. Vajtai, X. Wang, P. M. Ajayan, *Adv. Mater.* **2013**, *25*, 2452.
[26] P. Niu, L. Zhang, G. Liu, H.-M. Cheng, *Adv. Funct. Mater.* **2012**, *22*, 4763.
[27] X. Lu, K. Xu, P. Chen, K. Jia, S. Liu, C. Wu, *J. Mater. Chem. A* **2014**, *2*, 18924.
[28] X. Zhang, X. Xie, H. Wang, J. Zhang, B. Pan, Y. Xie, *J. Am. Chem. Soc.* **2013**, *135*, 18.
[29] X. Zhang, H. Wang, H. Wang, Q. Zhang, J. Xie, Y. Tian, J. Wang, Y. Xie, *Adv. Mater.* **2014**, *26*, 4438.
[30] Y. Cui, Z. Ding, P. Liu, M. Antonietti, X. Fu, X. Wang, *Phys. Chem. Chem. Phys.* **2012**, *14*, 1455.
[31] J. He, J. Wang, Y. Chen, J. Zhang, D. Duan, Y. Wang, Z. Yan, *Chem. Commun.* **2014**, *50*, 7063.
[32] Y. Zheng, L. Lin, X. Ye, F. Guo, X. Wang, *Angew. Chem. Int. Ed.* **2014**, *53*, 1.
[33] R. Li, J. Hu, M. Deng, H. Wang, X. Wang, Y. Hu, H.-L. Jiang, J. Jiang, Q. Zhang, Y. Xie, Y. Xiong, *Adv. Mater.* **2014**, *26*, 4783.